ARTICLE

Nickel Ferrite Aerogels with Monodisperse Nanoscale Building Blocks—The Importance of Processing Temperature and Atmosphere

Katherine A. Pettigrew,[†,⊥] Jeffrey W. Long,[†,*] Everett E. Carpenter,[§] Colin C. Baker,[†] Justin C. Lytle,[†] Christopher N. Chervin,[†] Michael S. Logan,[†] Rhonda M. Stroud,[‡] and Debra R. Rolison[†,*]

[†]Surface Chemistry Branch (Code 6170) and [‡]Materials and Sensors Branch (Code 6360), U.S. Naval Research Laboratory, 4555 Overlook Avenue SW, Washington, D.C. 20375, and [§]Department of Chemistry, Virginia Commonwealth University, Richmond, Virginia 23284. [⊥]Current address: Department of Chemistry, George Mason University, Fairfax, Virginia 22030.

ABSTRACT Using two-step (air/argon) thermal processing, sol—gel-derived nickel—iron oxide aerogels are transformed into monodisperse, networked nanocrystalline magnetic oxides of $NiFe_2O_4$ with particle diameters that can be ripened with increasing temperature under argon to 4.6, 6.4, and 8.8 nm. Processing in air alone yields poorly crystalline materials; heating in argon alone leads to single phase, but diversiform, polydisperse $NiFe_2O_4$, which hampers interpretation of the magnetic properties of the nanoarchitectures. The two-step method yields an improved model system to study magnetic effects as a function of size on the nanoscale while maintaining the particles within the size regime of single domain magnets, as networked building blocks, not agglomerates, and without stabilizing ligands capping the surface.

KEYWORDS: nickel ferrites · magnetic nanomaterials · nanoarchitectures · aerogels · sol—gel chemistry · single magnetic domains · thermal processing

Of the factors that influence the structural, physical, and chemical properties of nanoparticles, shape is among the most crucial.[1–4] For example, the magnetic properties of such materials as ferrites[5–9] and transition metal ferrites (MFe_2O_4),[10–13] are strongly affected by particle shape, as well as size.[14–16] Shape anisotropy provides a means to alter the magnetic properties of a given magnetic material.[2] Recently, Wang *et al.* found that the saturation magnetization of magnetic ferrites decreased with increasing shape anisotropy as the material was thermally transformed from particles of mixed shapes (diversiform) to nanowires and fibrous nanostructures.[7] A similar result was reported for multipodal copper ferrites relative to spherical $CuFe_2O_4$ particles.[12]

Nanoscale nickel ferrites, in particular, can exhibit irregular morphology and agglomerated particles as a consequence of postsynthetic processing.[17–21] The continued advancement and application of the transition metal ferrites as well as new ferromagnetic nanomaterials requires a more fundamental understanding of the effect of shape and size polydispersity on magnetic properties. Also necessary is the development of practical procedures to achieve magnetic nanomaterials with more uniform morphologies. In this report we describe synthetic and processing protocols that produce pore—solid nanoarchitectures of crystalline nickel ferrite, $NiFe_2O_4$, with size and shape monodispersity, which affords materials that are closer to the ideal for advanced magnetic applications.

RESULTS AND DISCUSSION

Effect of Thermal Processing on Size, Morphology, And Physical Properties. Amorphous transition metal ferrites ($M^{II}FeO_x$) are readily synthesized as highly porous, nanostructured aerogel monoliths by epoxide-driven sol–gel chemistry using metal chloride salts as precursors and supercritical CO_2 processing of the wet gels.[9,10,22,23] These materials are then transformed at controlled temperature and atmosphere into nanocrystalline ultraporous nanoarchitectures in which the solid network comprises nonagglomerated, inverse spinel nickel ferrite nanoparticles that are free of organic capping moieties. The particular thermal processing methods chosen to convert the amorphous aerogel into the crystalline aerogel are key to achieving size and shape monodispersity (see Experimental Methods for details on the synthesis).

We find that establishing networked nickel ferrite nanoparticles with controlled

*Address correspondence to jeffrey.long@nrl.navy.mil, rolison@nrl.navy.mil.

Received for review October 7, 2007 and accepted March 18, 2008.

Published online April 22, 2008. 10.1021/nn7002822 CCC: $40.75

size, a high degree of crystallinity, and a single morphology requires a two-step thermal protocol: calcination in air at 300 °C followed by heating in argon at 300 °C (300-AIR/300-ARG; Figure 1a). Heating $NiFeO_x$ aerogels in argon alone leads to highly crystalline nanoparticles, but of multiple shapes (300-ARG; Figure 1b). Heating in air alone leads to uniform, less-well crystallized nanoparticles (300-AIR; Figure 1c). The physical properties of the variously processed aerogels are summarized in Table 1.

The 300-ARG $NiFe_2O_4$ nanoarchitecture consists of two distinct morphologies (Figure 1b): irregular round particles with diameters of ~5 to 10 nm, and well-faceted polyhedra of ~25 nm on a side. Electron diffraction and lattice image data confirm that the particles of both morphologies exhibit the spinel crystal structure. X-ray powder diffraction analysis of the bulk sample confirms that the material exhibits spinel crystal structure with no mixed phases detectable (see Supporting Information, Figure S1). The XRD-determined crystallite size is 15 nm, as evaluated from the major diffraction peak (311) and the Scherrer equation. But as the TEM study shows, this material actually exhibits two particle morphologies with bimodal sizes grouped at 5 and 25 nm, thereby highlighting the limitation of XRD analysis of nanophase materials in order to establish size and shape information.

The saturation magnetization, M_S, of 300-ARG $NiFe_2O_4$ at 77 K is 49.3 emu g^{-1} (Figure 2), which approaches the 54.3 emu g^{-1} of bulk $NiFe_2O_4$ at 77 K.[24] Although this ferrite nanoarchitecture is highly crystalline and highly magnetic, it is difficult to correlate magnetic contributions to the physical attributes of the nanoparticles in such a diversiform, heterogeneous system. The magnetic response is likely dominated by the >20-nm polyhedra.

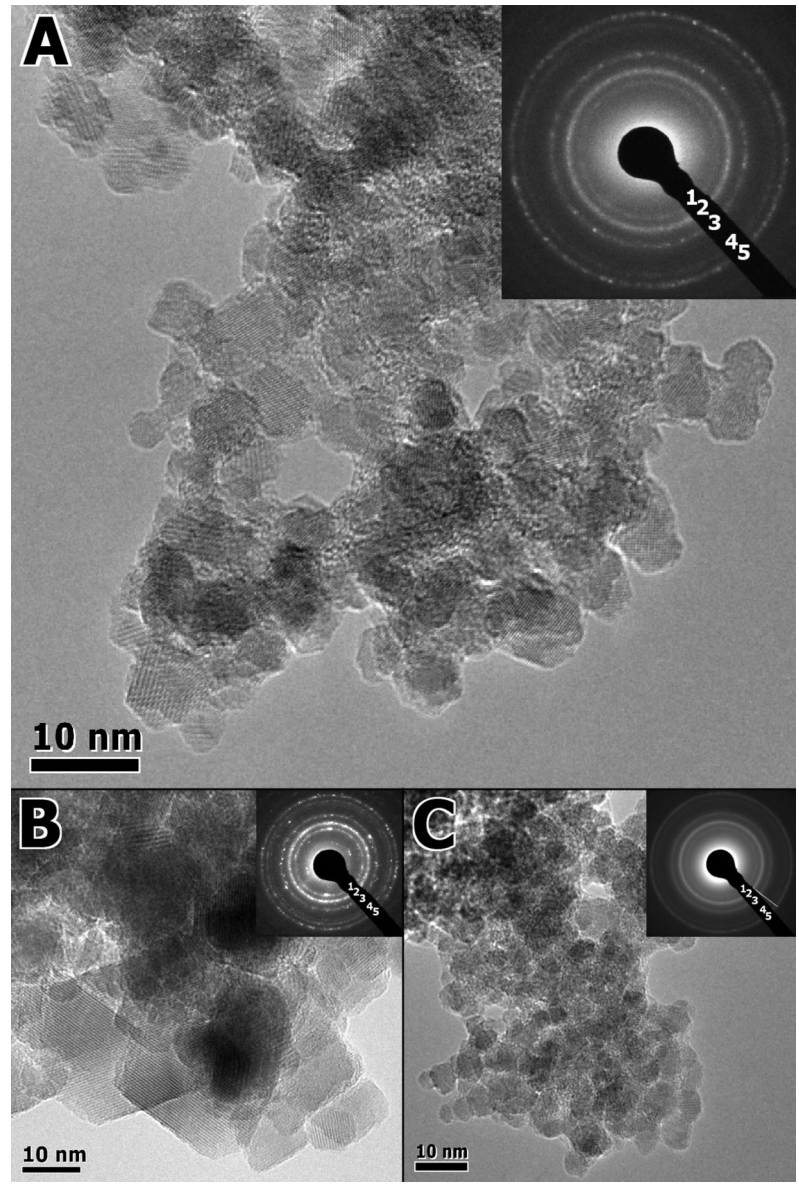

Figure 1. Transmission electron microscopy of the 300-AIR/300-ARG (A), 300-ARG (B), and 300-AIR (C) samples. The labels on the insets correspond to (1) (220), (2) (311), (3) (400), (4) (422) and (511), and (5) (440) spacings of the nickel ferrite spinel crystal structure.

Processing the amorphous aerogel in air at the same temperature yields a very different material: 300-AIR $NiFe_2O_4$ presents a single morphology where the network consists of roughly spherical 4.2 ± 1.0 nm particles (Figure 1c). This form of the ferrite approaches a saturation magnetization of only 23.2 emu g^{-1} at 77 K, consistent with the fact that such small particles typically exhibit markedly lower magnetization than the bulk material.[25] The inability of the mass-normalized

TABLE 1. Physical Properties of Nickel Ferrite Aerogels as a Function of Thermal Treatment

temperature—atmosphere of treatment	surface area [m^2 g^{-1}]	cumulative pore volume [cm^3 g^{-1}]	mean pore diameter [nm]	particle size by TEM [nm][a,b]
as-prepared	552	3.26	18	amorphous
300-ARG	103	0.96	27	5—25, diversiform
300-AIR	183	0.86	14	4.2 ± 1.0
300-AIR/300-ARG	181	1.06	15	4.6 ± 1.0
300-AIR/350-ARG	138	0.93	18	6.4 ± 1.4
300-AIR/400-ARG	86	0.57	26	8.8 ± 2.1

[a]The networked character of the nickel ferrite nanoparticles (*i.e.*, not agglomerated) was verified by scanning electron microscopy, Figure 5. [b]To determine the range in particle size for each sample, at least 200 particles were micrographically analyzed.

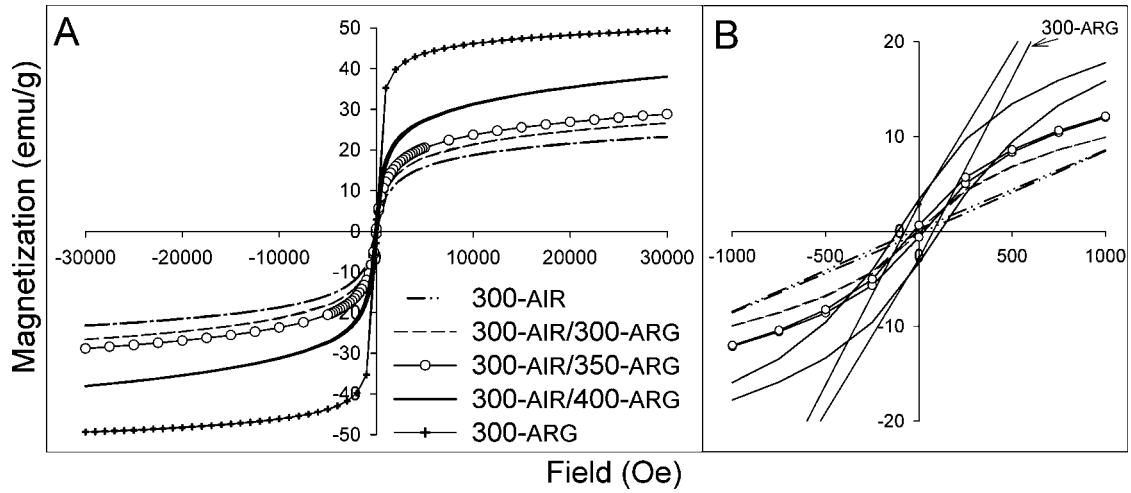

Figure 2. (A) SQUID M(H) measurements at 77 K for nickel ferrite aerogels processed using various thermal treatments; (B) magnified scale for the same data near zero applied field.

M_S of nanomaterials to match that of the bulk form reflects a magnetically silent layer at the surface of nanoparticles, with M_S tracking the surface-to-volume ratio (*i.e.*, an inverse particle size effect is found).[26] The fact that the magnetization of these particles does not fully saturate also correlates well with the poor crystallinity and low blocking temperature (see Table 2) of this form of the material.

Our previous work with magnetic iron oxide aerogels taught us that thermal processing under an inert atmosphere is critical in order to realize highly crystalline nanoparticles.[9] When the air treatment is followed by an argon treatment (300-AIR/300-ARG $NiFe_2O_4$), the nanoparticle morphology remains roughly spherical, the average particle size increases only slightly to 4.6 ± 1.0 nm, and the electron diffraction is sharper and the lattice fringes are more well-defined (Figure 1a) in comparison to 300-AIR $NiFe_2O_4$ (Figure 1c). The saturation magnetization at 77 K increases 15% to 26.6 emu g^{-1}, which because the morphology remains single-shaped and the particle size increases by 9.5%, likely arises from the combination of the more crystalline structure of the doubly processed ferrite and its slightly lower surface-to-volume ratio.

The effects of air (oxidizing) *versus* argon (inert/deoxygenating) thermal treatments on the as-synthesized $NiFeO_x$ aerogel were assessed by simultaneous thermogravimetric analysis (TGA) and differential scanning calorimetry (DSC). Weight loss proceeds in multiple steps with increasing temperature under both atmospheres, but a more rapid decrease in weight occurs under air (Figure 3). The DSC in dynamic air is dominated by a convolved, broad exotherm from 150−320 °C with concomitant evolution of CO_2 and organic byproducts from the initial sol−gel process (confirmed by mass spectrometric analysis of the evolving gases, Figure S2). Under flowing argon, the material exhibits a single exotherm at ~300 °C concomitant with the evolution of organic byproducts; the sharpness of the exotherm indicates it also represents crystallization of the nanomaterial.

To demonstrate that a single thermal treatment at 300 °C under air effectively removes organic byproducts of the synthesis, we collected TGA−DSC data for 300-AIR $NiFe_2O_4$ under flowing argon (Figure S3). The weight loss in argon from 300 to 400 °C is only ~0.9%, which matches the buoyancy factor of the instrument, while the DSC trace in this thermal processing range is peak-free. The results from both thermal methods indicate that the time the samples spend under argon at and above 300 °C contributes only to crystallite growth and not to loss of mass ascribable to organic byproducts.

Effect of Size on the Magnetic Properties of Networked, Shape-Controlled Nanoparticles. To explore the effect of size on the magnetic behavior of $NiFe_2O_4$ nanoarchitectures while retaining single-shaped, networked nanoparticles, the initial, critical thermal treatment in air at

TABLE 2. Magnetic Properties of Nickel Ferrite Aerogels as a Function of Thermal Treatment.

temperature−atmosphere of treatment	particle size by TEM [nm] [a]	T_B at 100 Oe [K]	T_B at 1000 Oe [K]	H_C at 77 K [Oe]	M_R at 77 K [emu g^{-1}]	M_S at 77 K [emu g^{-1}]
300-ARG	5−25	215	60	79	2.86	49.3
300-AIR	4.2 ±1.0	60	50	29	0.243	23.2
300-AIR/300-ARG	4.6 ±1.0	75	60	10	0.146	26.6
300-AIR/350-ARG	6.4 ±1.4	95	80	28	0.639	28.8
300-AIR/400-ARG	8.8 ±2.1	160	115	113	3.37	38.0

[a] To determine the range in particle size for each sample, at least 200 particles were micrographically analyzed.

300 °C was followed by an argon treatment to higher temperature: 350 and 400 °C. The 300-AIR/350-ARG and 300-AIR/400-ARG $NiFe_2O_4$ aerogels maintain roughly spherical morphology but show crystallite growth to 6.4 ± 1.4 nm and 8.8 ± 2.1 nm, respectively, with discernible edges visible by TEM for the networked nanoparticles in 300-AIR/400-ARG $NiFe_2O_4$ aerogels. The saturation magnetization increases slightly (to 28.8 emu g^{-1}) for 300-AIR/350-ARG $NiFe_2O_4$ and dramatically (to 38.0 emu g^{-1}) for 300-AIR/400-ARG $NiFe_2O_4$; the differing degree of magnetization at low field between the thermally ripened nanoarchitectures can be more readily discerned in Figure 2b. The calcined $NiFe_2O_4$ nanoarchitectures follow the trend reported for the effect of the surface-to-volume ratio on saturation magnetization of other nanomaterials:[26] a monotonic increase in M_S is obtained as the surface-to-volume ratio decreases; see Figure S4.

For nanoparticles, the transition to a single magnetic domain occurs below a specific size that is unique to the material and its geometry. In the single-domain regime, magnetization reversal is controlled by coherent rotation of all magnetic moments in the sample, an energetically costly process. The coercivity, H_c, tracks the size of the nanoparticle, with a peak occurring at the transition to a single magnetic domain.[27] Decreases in particle size yield large decreases in coercivity until the superparamagnetic limit is reached in which thermal energy dominates. The result is a temperature- and field-dependent magnetic blocking temperature, T_B, with the absence of both coercivity H_c and remanent magnetization at temperatures above T_B.[28]

Our control over shape and size of the networked $NiFe_2O_4$ nanoparticles is further observed in field-cooled and zero field-cooled measurements and magnetization hysteresis loops. The size limit for a single magnetic domain in nickel ferrite has been shown to be 13 nm at 80 K.[29] After heat treatments, even to 400 °C, our materials remain small enough to exist as single magnetic domains at 77 K. All of our ferrite nanoarchitectures exhibit blocking phenomena characteristic of superparamagnetic materials. The 300-AIR/300-ARG $NiFe_2O_4$ with 4.6-nm particles has a coercivity of 10 Oe at 77 K (bulk $NiFe_2O_4$ has a coercivity of 13.7 Oe[24]) with a small remanent magnetization, M_r, of 0.146 emu g^{-1}. The T_B for this sample is 75 K at 100 Oe, decreasing to 60 K at 1000 Oe. The nonzero values of H_c and M_r occur because the magnetic measurements were performed close to T_B for this sample.

The blocking temperature for the 300 °C-calcined $NiFe_2O_4$ nanoparticle networks after thermal ripening in dynamic argon, as measured at a field strength of 100 Oe, increases from 75 K (300-AIR/300-ARG) to 95 K (300-AIR/350-ARG) to 160 K (300-AIR/400-ARG). This increase in T_B is expected because of the respective increase in crystallite size from 4.6 to 6.4 to 8.8 nm and is accompanied by increasing values of coercivity at 77 K (Table 2); doubling the particle size (from 4.6 to 8.8 nm) leads to an order of magnitude increase in coercivity.

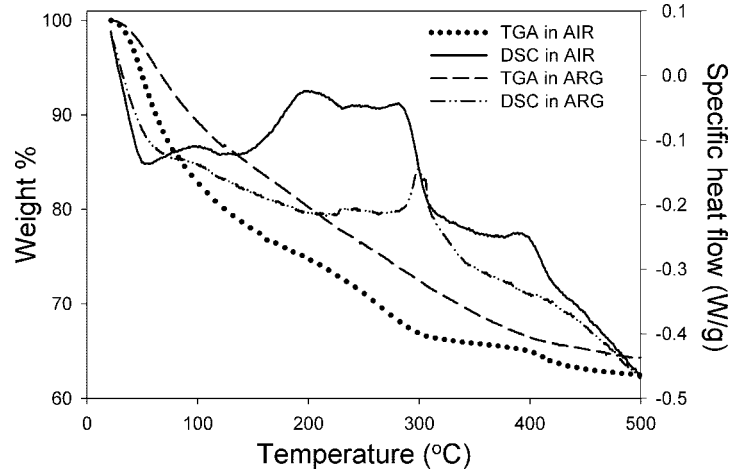

Figure 3. Thermal analysis of as-prepared nickel ferrite aerogel *via* simultaneous thermogravimetric (TGA) and differential scanning calorimetry (DSC) in either air or flowing argon. Measurements are performed with a 1 °C min^{-1} heating ramp.

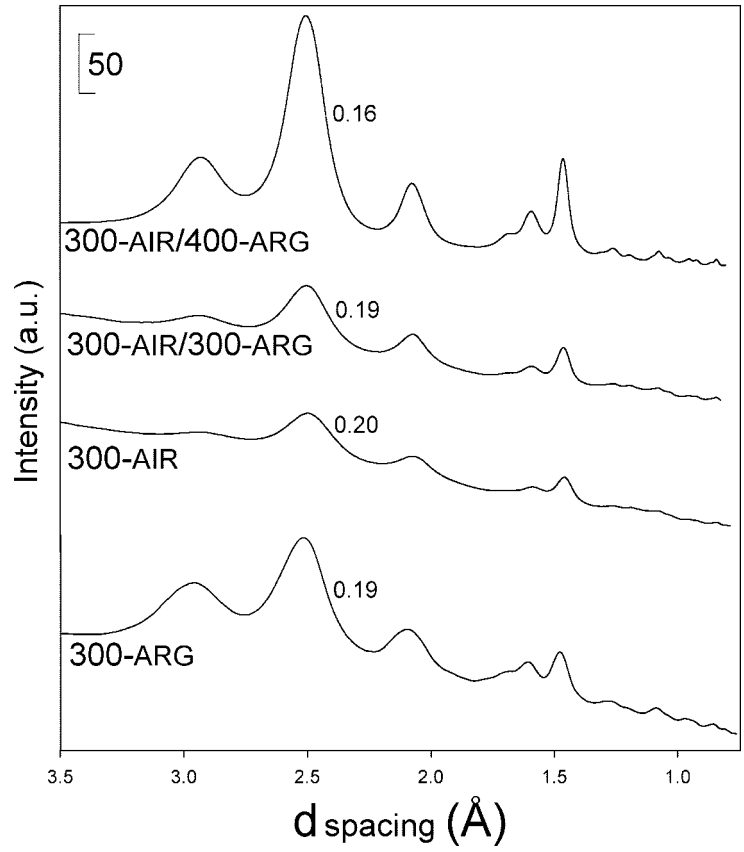

Figure 4. Radially averaged line profiles of the selected-area electron diffraction patterns from the three samples presented in Figure 1 plus a 300-AIR/400-ARG sample; the values for the full-width at half-maximum of the (311) reflection are noted next to the (311) line for all four nanoarchitectures.

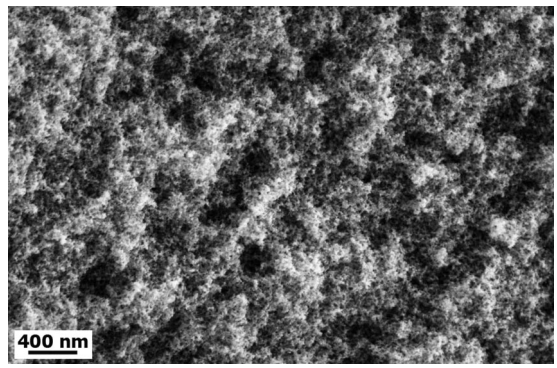

Figure 5. Scanning electron micrograph of the 300-AIR/300-ARG nickel ferrite aerogel demonstrating the character of the aerogel nanoarchitecture as highly porous with nonagglomerated nanoparticles.

Blocking phenomena are also possible when exchange interactions occur, such as for core−shell nanoparticles where an exchange bias shifts the hysteresis loop.[30,31] Core−shell behavior for nickel ferrite nanoparticles has been observed by others to exhibit hysteresis loop shifts,[32] as well as unclosed loops,[33] and a lack of saturation at high field for tests below the sample blocking temperature.[33] We do not see any of these effects in our measurements, further indicating that the nanoparticles in the network act as single domain structures. The slope of the ZFC curve for our aerogel samples is consistent with interacting grains,[34] which also indicates that we do not have core−shell structures. This result is supported by our Mössbauer work with single-phase maghemite (γ-Fe_2O_3) aerogels in which the networked nanoparticles are magnetically interacting.[23]

No physical abnormalities at the surface of the networked nanoparticles are evident by HRTEM as lattice fringes are observed to the edge of the particles. The electron and X-ray diffraction patterns indicate only a single phase is present (*i.e.*, no intermixed or phase-separated iron oxide/nickel oxide phases are present). Line profiles derived from the selected-area electron diffraction (SAED) patterns of all forms of the nickel ferrite nanoarchitectures confirm the absence of phase separation upon thermal processing (Figure 4). The characteristic peaks of $NiFe_2O_4$ are present in the line profiles and match the JCPDS data (03-0875) for inverse spinel ferrite. In particular, the increasing intensity of the (311) reflection and its decreasing full-width at half-maximum tracks the increase in the size of the $NiFe_2O_4$ crystallites with increasing temperature under argon.

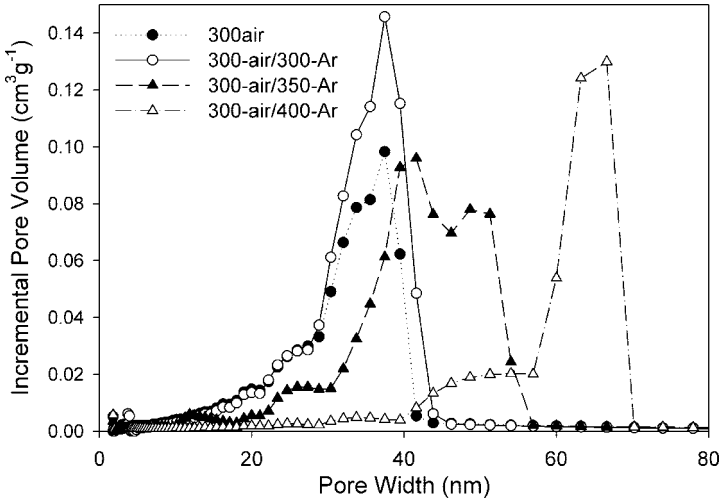

Figure 6. Pore-size distribution plots for heat-treated nickel ferrite aerogels as determined by N_2 porosimetry. These plots are generated using a Broekhoff−de Boer model fitting (cylindrical pore geometry) of the experimental adsorption isotherms.

Characterization of the Pore Network in $NiFe_2O_4$ Aerogels. The ability to control the size and shape of the nanoscale building blocks in these highly porous magnetic architectures will be critical for applications such as field-assisted separations and catalysis. A correlating requirement for such applications is a high-quality pore network,[35] through which molecular reactants and analytes traverse the magnetized nanoarchitecture. Scanning electron microscopy verifies that the nickel ferrite architectures are nonagglomerated and highly porous (see Figure 5 for 300-AIR/300-ARG $NiFe_2O_4$). We also studied the specific surface area of the nickel ferrite network and porosity parameters for the nanoarchitecture using N_2 physisorption. The aerogel nanoarchitectures in all forms exhibit type-4 isotherms with H3-type hysteresis loops indicative of an interconnected network of mesopores.[36] The as-prepared $NiFeO_x$ monoliths exhibit the highest specific surface area (552 $m^2\ g^{-1}$) and cumulative pore volume (3.26 $cm^3\ g^{-1}$). After the initial 300 °C thermal treatment in air, the monoliths visibly densify, but retain high surface area (183 $m^2\ g^{-1}$) and pore volume (0.83 $cm^3\ g^{-1}$). The loss of pore volume relative to the as-prepared aerogel is primarily observed for pores between 40 and 80 nm, while pores $<$40 nm are preserved.

The 300 °C heat treatment in argon, following the air treatment, leaves the surface area and pore-size distribution unaffected (Table 1). Pore volume, however, increases to 1.06 $cm^3\ g^{-1}$, which can be attributed to initial sintering of the particle network without collapse of the pore network thereby yielding an increase in specific pore volume. Thermal treatments at 350 and 400 °C in argon progressively decrease the surface area and pore volume of the nanoarchitectures, but these changes are accompanied by a rearrangement in the pore-size distribution to larger pores. As the nanoparticles grow larger, they grow into the framework of the aerogel without collapsing it, which will allow us to retain the open pore network of the nanoarchitecture while poising the material to express different magnetic character.

Atmosphere and temperature play critical roles in controlling the crystallization of nickel ferrite nanoarchitectures. A two-step heat-treatment, first in air and then in argon, retains size and shape control of the net-

worked $NiFe_2O_4$ nanoparticles. The magnetic, porous solids when prepared to be monodisperse and single-shaped retain the desirable characteristics of aerogels (high surface area, nonagglomerated particles, and large pore volume), and do so even with thermal ripening of the networked $NiFe_2O_4$ nanoparticles. The measure of control we have achieved in this study permits such magnetic properties as remanence and coercivity to be increased by an order of magnitude merely by thermally ripening the networked nanoparticles by a factor of 2, while still maintaining the particles at <10 nm in size and therefore as single magnetic domains. These size- and shape-controlled nanoarchitectures provide an experimental model system that can be systematically explored for a host of applications susceptible to magnetic-field influences.

EXPERIMENTAL METHODS

Chemicals. Epichlorohydrin, 99+% (Aldrich), iron(III) chloride hexahydrate, 97% ACS reagent (Aldrich), nickel(II) chloride hydrate, 99.95% (Aldrich), anhydrous ethyl alcohol, 200 proof (Warner Graham), and acetone (Fisher) were used as received.

Synthesis and Processing of $NiFeO_x$ Aerogels. Nickel−iron oxide aerogels are prepared by minor modifications to our previously reported procedures for FeO_x and $MnFeO_x$ aerogels.[8,11] To a solution of 0.28 M (5.88 g) $FeCl_3 \cdot 6H_2O$ and 0.14 M (2.50 g) $NiCl_2 \cdot 6H_2O$ in 60 mL of anhydrous ethyl alcohol, 23.89 g (20.25 mL) epichlorohydrin (8:1 epoxide/metals ratio) is added with stirring. The solution is then stirred for 15 min, during which time it darkens from orange to a dark red/brown. The $NiFeO_x$ sol is then transferred into several cylindrical high-density polyethylene molds (Zinsser), which are sealed with plastic wrap and parafilm. Gelation occurs after ~45 min; the gels are then aged for 16 h, transferred to vials, and submerged in anhydrous ethanol. The solvent is exchanged over several days with two additional ethanol rinses followed by three rinses with acetone.

The acetone-filled gels are transferred under acetone into a critical-point dryer (Polaron Range, Quorum Technologies, New Haven, East Sussex) maintained at 10 °C, which is subsequently filled with liquid CO_2. After a series of pore-fluid exchanges with CO_2 (6-min flushes of CO_2 with equilibration for 20 min between flushes for a total of 36 min or longer if there is evidence of acetone in the CO_2 exhaust), the CO_2 level in the autoclave is adjusted to just cover the sample boat. The temperature within the autoclave is increased beyond the supercritical point of CO_2 (T_c = 31 °C; P_c = 7.4 MPa), followed by a slow venting of the supercritical CO_2, yielding brown aerogels that retain the dimensions of the wet gel.

The nickel ferrite monoliths were thermally processed in a fused quartz tube mounted in a Lindberg programmable tube furnace. Samples were heated to the desired temperature (300, 350, and 400 °C) by ramping at 1 °C min^{-1}, kept at temperature for 20 h, and then cooled to ambient temperature. Thermal treatments were performed in either static air or flowing argon; for the two-step process, the calcined aerogels were cooled to ambient under air before taking to the desired temperature under argon at 1 °C min^{-1}. The various samples are denoted according to their thermal treatments (Table 1).

Physical Characterization. ***Thermal Analysis.*** The ferrites were analyzed *via* simultaneous thermogravimetric analysis (TGA) and differential scanning calorimetry (DSC) at a rate of 1 °C min^{-1} in either flowing argon or ambient air (Rheometrics (STA 1500) simultaneous thermal analyzer). The gas-phase byproducts generated upon heating as-prepared $NiFeO_x$ aerogel in ambient air or argon were analyzed by simultaneous residual gas analysis (RGA) with a Pfeiffer Thermostar quadropole mass spectrometer coupled to the Rheometrics TGA−DSC by a silica capillary heated at 150 °C.

Electron Microscopy. A JEOL 2200FS transmission electron microscope (TEM) equipped with a Gatan CCD camera and Noran System Six EDS was used to characterize the aerogel morphologies, confirm particle size, and determine crystal structure. Samples were prepared by dry-grinding the aerogel powders then brushing the dust onto holey-carbon film supports. We examine multiple areas of order 100 μm × 100 μm from each sample to ensure that the images we obtain are representative. Scanning electron microscopy (SEM; Carl Zeiss Supra 55) was used to characterize the networked or agglomerated nature of the materials. For analysis, the specimen was prepared by attaching a small portion of the aerogel monolith to an aluminum stub using conductive silver epoxy (Circuit Works). The epoxy was then cured at room temperature in air for 1 h followed by heating in air at 100 °C for 2 h. The specimen was not sputter-coated prior to analysis.

X-ray Diffraction. The powder was packed into an aluminum holder. The samples were analyzed using either a Rigaku D Max-B or Bruker D8 Advance X-ray diffractometer. A 2θ survey scan was performed from 10° to 100° at 1° min^{-1} and a sample interval of 0.05°. The high-resolution scans were done on the (311) peak at 1° min^{-1} and a sample interval of 0.01°. The particle size was evaluated using the Scherrer formula, in which JADE fitting software fit the peak to a Pearson VII function to determine the fwhm of the peak. The software eliminated machine broadening and the Cu K-α2 peak.

Magnetic Measurements. Samples were prepared in a gelatin capsule according to literature techniques, adjusted for sample holder background,[37] and analyzed using a Quantum Design MPMS 5S SQUID magnetometer. The saturation magnetization was determined at the highest field employed.

Porosimetry. Surface area and porosities were determined by nitrogen physisorption using a Micromeritics ASAP2010 accelerated surface area and porosimetry analyzer. All samples were degassed at 80 °C for at least 24 h prior to characterization, except for the as-prepared aerogel, which was degassed at 50 °C for at least 48 h. Pore-size distributions were calculated from adsorption isotherm data using Micromeritics DataMaster software (DFT−Broekhoff−de Boer model, classical cylindrical pore geometry).

Acknowledgment. This work was supported by the Office of Naval Research Laboratory. K.A.P. (2004−2007) and C.N.C. (2006−2009) are NRC Postdoctoral Associates; J.C.L. (2007−2008) is an ASEE Postdoctoral Associate.

Supporting Information Available: X-ray powder diffraction analysis results of the bulk sample; MS data; TGA−DSC data; Figures S1−S4. This material is available free of charge *via* the Internet at http://pubs.acs.org.

REFERENCES AND NOTES

1. Puntes, V. F.; Krishnan, K. M.; Alivisatos, A. P. Colloidal Nanocrystal Shape and Size Control: The Case of Cobalt. *Science* **2001**, *291*, 2115–2117.
2. Hyeon, T. Chemical Synthesis of Magnetic Nanoparticles. *Chem. Commun.* **2003**, 927–934.
3. Burda, C.; Chen, X.; Narayanan, R.; El-Sayed, M. A. Chemistry and Properties of Nanocrystals of Different Shapes. *Chem. Rev.* **2005**, *105*, 1025–1102.
4. Zhao, L.; Zhang, H.; Xing, Y.; Song, S.; Yu, S.; Shi, W.; Guo, X.; Yang, J.; Lei, Y.; Cao, F. Morphology-Controlled Synthesis of Magnetites with Nanoporous Structures and Excellent Magnetic Properties. *Chem. Mater.* **2008**, *20*, 198–204.
5. Hyeon, T.; Lee, S. S.; Park, J.; Chung, Y.; Na, H. B. Synthesis of Highly Crystalline and Monodisperse Maghemite Nanocrystallites without a Size-Selection Process. *J. Am. Chem. Soc.* **2001**, *123*, 12798–12801.

6. Xu, X. N.; Wolfus, Y.; Shaulov, A.; Yeshurun, Y.; Felner, I.; Nowik, I.; Koltypin, Y.; Gedanken, A. Annealing Study of Fe_2O_3 Nanoparticles: Magnetic Size Effects and Phase Transformations. *J. Appl. Phys.* **2002**, *91* (7), 4611–4616.
7. Yang, S.; Yi, J.-H.; Son, S.; Jang, J.; Altman, I. S.; Pikhitsa, P. V.; Choi, M. Fragmentation of Fe_2O_3 Nanoparticles Driven by a Phase Transition in a Flame and Their Magnetic Properties. *Appl. Phys. Lett.* **2003**, *83*, 4842–4844.
8. Wang, J.; Chen, Q.; Zeng, C.; Hou, B. Magnetic-Field-Induced Growth of Single-Crystalline Fe_3O_4 Nanowires. *Adv. Mater.* **2004**, *16*, 137–140.
9. Long, J. W.; Logan, M. S.; Rhodes, C. P.; Carpenter, E. E.; Stroud, R. M.; Rolison, D. R. Nanocrystalline Iron Oxide Aerogels as Mesoporous Magnetic Architectures. *J. Am. Chem. Soc.* **2004**, *126*, 16879–16889.
10. Chen, Q.; Zhang, Z. J. Size-Dependent Superparamagnetic Properties of $MgFe_2O_4$ Spinel Ferrite Nanocrystallites. *Appl. Phys. Lett.* **1998**, *73* (21), 3156–3158.
11. Sun, S. H.; Zeng, H.; Robinson, D. B.; Raoux, S.; Rice, P. M.; Wang, S. X.; Li, G. X. Monodisperse MFe_2O_4 (M = Fe, Co, Mn) Nanoparticles. *J. Am. Chem. Soc.* **2002**, *126*, 273–279.
12. Long, J. W.; Logan, M. S.; Carpenter, E. E.; Rolison, D. R. Synthesis and Characterization of Mn-FeOx Aerogels with Magnetic Properties. *J. Non-Cryst. Solids* **2004**, *350*, 182–188.
13. Zhang, Y. Q.; Huang, Z. B.; Tang, F. Q.; Ren, J. Preparation and Shape Control of Multiple-Arm Magnetic Particles. *Solid State Commun.* **2006**, *138*, 132–135.
14. McHenry, M. E.; Laughlin, D. E. Nano-Scale Materials Development for Future Magnetic Applications. *Acta Mater.* **2000**, *48*, 223–238.
15. Park, J.-I.; Kang, N.-J.; Jun, Y.-W.; Oh, S. J.; Ri, H.-C.; Cheon, J. Superlattice and Magnetism Directed by the Size and Shape of Nanocrystals. *ChemPhysChem* **2002**, *6*, 543–547.
16. Wei, X.-W.; Zhu, G.-X.; Zhou, J.-H.; Sun, H.-Q. Solution Phase Reduction to Fe−Ni Alloy Nanostructures with Tunable Shape and Size. *Mater. Chem. Phys.* **2006**, *100*, 481–485.
17. Cheng, Y.; Zheng, Y.; Wang, Y.; Bao, F.; Qin, Y. Synthesis and Magnetic Properties of Nickel Ferrite Nano-Octahedra. *J. Solid State Chem.* **2005**, *178*, 2394–2397.
18. Son, S.; Taheri, M.; Carpenter, E.; Harris, V. G.; McHenry, M. E. Synthesis of Ferrite and Nickel Ferrite Nanoparticles Using Radio-Frequency Thermal Plasma Torch. *J. Appl. Phys.* **2002**, *91*, 7589–7591.
19. Zhou, J.; Ma, J.; Sun, C.; Xie, L.; Zhao, Z.; Tian, H.; Wang, Y.; Tao, J.; Zhu, X. Low-Temperature Synthesis of $NiFe_2O_4$ by a Hydrothermal Method. *J. Am. Ceram. Soc.* **2005**, *88*, 3535–3537.
20. Wang, J. Prepare Highly Crystalline $NiFe_2O_4$ Nanoparticles with Improved Magnetic Properties. *Mater. Sci. Eng., B* **2006**, *127*, 81–84.
21. Lee, P. Y.; Ishizaka, K.; Suematsu, H.; Jiang, W.; Yatsui, K. Magnetic and Gas Sensing Property of Nanosized $NiFe_2O_4$ Powders Synthesized by Pulsed Wire Discharge. *J. Nanoparticle Res.* **2006**, *8*, 29–35.
22. Gash, A. E.; Tillotson, T. M.; Satcher, J. H.; Poco, J. F.; Hrubesh, L. W.; Simpson, R. L. Use of Epoxides in the Sol−Gel Synthesis of Porous Iron(III) Oxide Monoliths from Fe(III) Salts. *Chem. Mater.* **2001**, *13*, 999–1007.
23. Carpenter, E. E.; Long, J. W.; Rolison, D. R.; Logan, M. S.; Stroud, R. M.; Logan, M. S.; Theilu Kuhn, L.; Rosendahl Hansen, B.; Mørup, S. Magnetic and Mössbauer Spectroscopy Studies of Nanocrystalline Iron Oxide Aerogels. *J. Appl. Phys.* **2006**, *99*, 08N711-1–08N711-3.
24. Smitz, J.; Wijn, H. P. J. *Ferrites: Physical Properties of Ferromagnetic Oxides in Relation to Their Technical Applications*; John Wiley and Sons: New York, 1959.
25. Morrish, A. H.; Haneda, K. Magnetic Structure of Small $NiFe_2O_4$ Particles. *J. Appl. Phys.* **1981**, *52*, 2496–2498.
26. Tang, Z. X.; Sorensen, C. M.; Klabunde, K. J.; Hadjipanayis, G. C. Size-Dependent Curie-Temperature in Nanoscale $MnFe_2O_4$ Particles. *Phys. Rev. Lett.* **1991**, *67*, 3602–3605.
27. Klabunde, K. J. *Nanoscale Materials in Chemistry*; Wiley Interscience: New York, 2001.
28. Aharoni, A. *Introduction to the Theory of Ferromagnetism*, 2nd ed.; Oxford University Press: New York, 2000.
29. George, M.; John, A. M.; Nair, S. S.; Joy, P. A.; Anantharaman, M. R. Finite Size Effects on the Structural and Magnetic Properties of Sol−Gel Synthesized $NiFe_2O_4$ Powders. *J. Magn. Magn. Mater.* **2006**, *302*, 190–195.
30. Meiklejohn, W. H. Exchange Anisotropy−A Review. *J. Appl. Phys.* **1962**, *33*, 1328–1335.
31. Martinez, B.; Obradors, X.; Balcells, L.; Rouanet, A.; Monty, C. Low Temperature Surface Spin-Glass Transition in γ-Fe_2O_3 Nanoparticles. *Phys. Rev. Lett.* **1998**, *80*, 181–184.
32. Sepalak, V.; Bergmann, I.; Feldhoff, A.; Heitjans, P.; Krumeich, F.; Menzel, D.; Litterst, F. J.; Campbell, S. J.; Becker, K. D. Nanocrystalline Nickel Ferrite, $NiFe_2O_4$: Mechanosynthesis, Nonequilibrium Cation Distribution, Canted Spin Arrangement, and Magnetic Behavior. *J. Phys. Chem. C* **2007**, *111*, 5026–5033.
33. Kale, A.; Gubbala, S.; Misra, R. D. K. Magnetic Behavior of Nanocrystalline Nickel Ferrite Synthesized by the Reverse Micelle Technique. *J. Magn. Magn. Mater.* **2004**, *277*, 350–358.
34. Papusoi, C., Jr.; Stancu, A.; Dormann, J. L. The Initial Susceptibility in the FC and ZFC Magnetisation Processes. *J. Magn. Magn. Mater.* **1997**, *174*, 236–246.
35. Rolison, D. R. Catalytic Nanoarchitectures−The Importance of Nothing and the Unimportance of Periodicity. *Science* **2003**, *299*, 1698–1701.
36. Webb, P. A.; Orr, C. *Analytical Methods in Fine Particle Technology*; Micromeritics Instrument Corp.: Norcross, GA, 1997.
37. O'Connor, C. J. Magnetochemistry−Advances in Theory and Experimentation. *Progr. Inorg. Chem.* **1982**, *29*, 203–283.